Research Square

Preprints are preliminary reports that have not undergone peer review.
They should not be considered conclusive, used to inform clinical practice,
or referenced by the media as validated information.

Interfacial thermal response and bonding behavior of CF/PEEK composites joined by tangential ultrasonic welding without energy directors

Zhongliang Cao

caoliang@jsut.edu.cn

Jiangsu University of Technology

Fanyang Liu

Jiangsu University of Technology

Leiming Chen

China Machinery Academy Group Jiangsu Branch Co., Ltd.

Jiazeng Pan

Jiangsu University of Technology

Zhichuan Lin

Jiangsu University of Technology

Jintao Gu

Jiangsu University of Technology

Research Article

Keywords: CF/PEEK composites, Ultrasonic welding without energy directors, Tangential vibration, Interfacial thermal response, Fracture morphology, Lap shear strength

Posted Date: November 20th, 2026

DOI: https://doi.org/10.21203/rs.3.rs-11449047/v1

License: This work is licensed under a Creative Commons Attribution 4.0 International License.
Read Full License

Interfacial thermal response and bonding behavior of CF/PEEK composites joined by tangential ultrasonic welding without energy directors

Zhongliang Cao[1]*, Fanyang Liu[1], Leiming Chen[2], Jiazeng Pan[1], Zhichuan Lin[1] and Jintao Gu[1]

[1] School of Mechanical Engineering, Jiangsu University of Technology, Changzhou 213000, Jiangsu, China

[2] China Machinery Academy Group Jiangsu Branch Co., Ltd., Changzhou 213000, Jiangsu, China

*Corresponding author: Zhongliang Cao. E-mail: caoliang@jsut.edu.cn.

Acknowledgements

ChatGPT (OpenAI) assisted with translation, language editing, manuscript organization, reference formatting, and figure presentation. The authors retain responsibility for the scientific content and its verification against the original research records.

Funding statement

This study was supported by the Universities Natural Science Research Major Project of Jiangsu Province (Grant No. 21KJA460004) and the National Natural Science Foundation of China (Grant No. 51705266).

Abstract

Tangential ultrasonic welding without energy directors places carbon fiber-reinforced polyether ether ketone (CF/PEEK) laminates in direct contact. The spatial distribution of interfacial bonding provides a basis for understanding joint load-bearing performance. This study combines an interfacial frictional heating model, lap shear testing, industrial computed tomography (CT) of representative joints, and fracture-surface observations. Thermal responses and bonding characteristics are compared across welding force, amplitude, and time series. The calculations locate high-temperature regions mainly at the overlap edges and predict higher edge temperature peaks with increasing amplitude. At 150 N and a single-sided amplitude of 12 μm, the 800 ms joint reached the highest measured apparent lap shear strength, 9.84 MPa. Its effective fracture-surface area fraction was 46.0%. The corresponding values for the 1000 ms joint were 5.73 MPa and 32.9%, accompanied by local gaps and resin extrusion. Effective fracture-surface area fractions and strengths changed in the same direction in the amplitude and time series. The force series exhibited a different area–strength relationship. CT and microscopic fracture-surface observations linked these differences to interfacial continuity, local pores, and material damage. The results support assessing joints without energy directors through both effective fracture-surface coverage and local bonding conditions.

Keywords: CF/PEEK composites; Ultrasonic welding without energy directors; Tangential vibration; Interfacial thermal response; Fracture morphology; Lap shear strength

1 Introduction

Carbon fiber-reinforced polyether ether ketone (CF/PEEK) composites combine high specific strength with thermal and chemical resistance. These properties support lightweight structures for aerospace and advanced transportation applications [1,2]. The reprocessability and recyclability of the thermoplastic matrix also broaden manufacturing and maintenance options [3,4]. Structures assembled from laminate components require joining processes that transfer loads locally while controlling interfacial defects and matrix damage. Understanding interface formation and assessing joint quality during rapid joining are therefore relevant to CF/PEEK structural manufacturing [5,6].

Ultrasonic welding (UW) delivers energy to a joint through high-frequency mechanical vibration over a short period. It offers rapid joining, eliminates additional fasteners, and facilitates integration into automated manufacturing [4,7]. Interfacial friction and internal material dissipation generate heat that promotes bonding across polymer interfaces [8,9]. Energy directors concentrate local heat input, while their material and geometry also modify interfacial composition and heat transfer [10]. Welding without energy directors removes the separate interfacial layer. The initial contacting surfaces and loading conditions then jointly influence heat input and bond formation [7,11]. In tangential welding, vibration is applied parallel to the overlap interface. Relating internal joint structure to fracture-surface features helps interpret overall load-bearing performance in terms of local bonding conditions.

Previous studies have advanced CF/PEEK ultrasonic welding through interface design, process control, and thermal analysis. Bonmatin et al. [12] examined temperature histories and mechanical properties of joints containing polyetherimide (PEI) interfacial layers. Korycki et al. [13] compared interfacial characteristics and joint strengths under time and displacement control using integrated PEI energy directors. Tsiangou et al. [14] investigated the sensitivity of PEEK-based composite joints to welding force and amplitude. Numerical studies have described temperature evolution and analyzed frictional and viscoelastic heating [15,16]. Sonotrode geometry, process control, and combined simulation and experimentation have also been used to study joint quality [17,18]. Studies of bonding conditions and failure modes have connected joint performance to local interfacial features [19,20].

Recent interface-design studies have connected heat distribution with joint performance. Wang et al. examined temperature uniformity, defects, and fracture morphology in continuous-fiber CF/PEEK joints produced using embossed energy directors [21]. Li et al. used PEEK mesh energy directors for CF/PEEK spot and continuous

ultrasonic welding to investigate weld quality and uniformity [22]. For CF/epoxy–CF/PEI hybrid joints, Liu et al. used variable-flexibility energy directors to regulate heat generation at the interface edges and center [23]. Yang et al. investigated how the crystallinity of PEEK energy directors affects CF/PEEK welding quality and process stability [24]. These studies relate interfacial geometry and resin condition to local heating and bonding quality.

Studies without separate energy directors have focused on initial contact and local energy input. Liu et al. introduced an unsupported annular region for ring-focused ultrasonic welding of CF/PEEK and examined interfacial heating, weld area, and joint strength [25]. Wang et al. co-consolidated an extra resin layer on CF/PEI surfaces to improve interfacial resin supply and welding uniformity without additional energy directors [26]. These approaches modify local support conditions and interfacial resin configuration, respectively. They indicate that bond formation without separate energy directors should be interpreted in relation to the specific contact conditions and interface composition.

Building on this work, the present study examines directly contacting CF/PEEK interfaces under tangential vibration without separate energy directors. It focuses on the relationship between effective fracture-surface coverage and load-bearing performance across three parameter series. The different area–strength relationships are interpreted alongside internal structural features.

Welding force, single-sided amplitude, and welding time were varied to relate apparent lap shear strength to effective fracture-surface area fraction. Industrial CT and microscopic fracture-surface observations identified interfacial gaps, continuity, and local material damage. An interfacial frictional heating model calculated temperature histories and spatial distributions under the corresponding loading conditions. The analysis connects thermal response, interfacial structure, and load-bearing performance through bonding coverage and local bonding conditions. These relationships provide structural evidence for analyzing joining processes involving directly contacting CF/PEEK surfaces.

2 Materials and experimental methods

2.1 Materials and specimen preparation

CF/PEEK laminates were prepared from T700-grade continuous carbon fiber-reinforced PEEK prepreg. The nominal prepreg ply thickness was 0.125 mm, and the fiber volume fraction was approximately 52%. Compression molding produced laminates with a $[0/90]_2s$ lay-up and a thickness of approximately 1.0 mm. Figure 1 shows the molding temperature profile. The melting temperature of PEEK is approximately 343 °C [27]. Tables 1 and 2 list the mechanical and thermophysical properties of CF/PEEK, respectively.

Rectangular specimens measuring 100 mm × 20 mm were cut using a water jet. Two laminates formed a single-lap joint with an overlap length and width of 20 mm, giving a nominal overlap area of 400 mm^2. In Fig. 2(a), red identifies the welding region, and blue identifies the gripping regions for lap shear testing. The CF/PEEK surfaces were placed in direct contact during welding, without separate energy directors or additional resin layers.

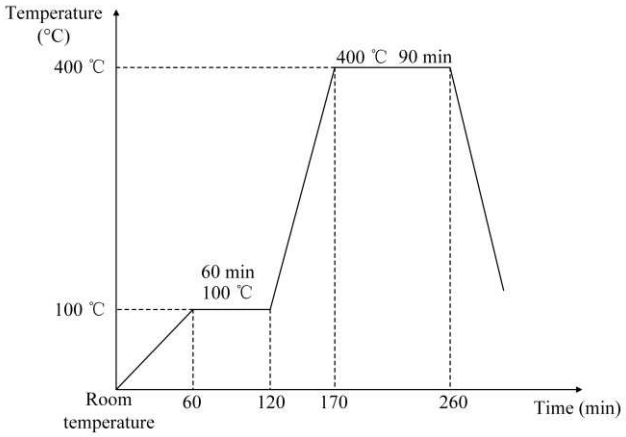

Fig. 1 Temperature profile used for laminate molding

Table 1. Mechanical properties of CF/PEEK

Temperature (°C)	E_1 **(GPa)**	$E_2 = E_3$ **(GPa)**	$\nu_{12} = \nu_{13} = \nu_{23}$	$G_{12} = G_{13}$ **(GPa)**	G_{23} **(GPa)**	**Density** ρ **(kg m^{-3})**
25	71.695	7.245	0.36	5.209	3.700	1600
100	63.913	6.458	0.36	4.644	3.298	1600
200	52.467	5.302	0.36	3.812	2.708	1600
300	38.846	3.925	0.36	2.822	2.005	1600
400	26.229	2.650	0.36	1.906	1.354	1600

Table 2. Thermophysical properties of CF/PEEK

Temperature (°C)	**Specific heat** C_p **(J kg^{-1} K^{-1})**	**Thermal conductivity** k **(W m^{-1} K^{-1})**	**90° thermal expansion coefficient** α_{90} **(K^{-1})**	**0° thermal expansion coefficient** α_0 **(K^{-1})**
25	823	0.460	—	—
100	1038	0.514	3.807×10^{-5}	0.670×10^{-6}
175	1265	0.556	3.965×10^{-5}	0.194×10^{-6}
250	1460	0.540	4.812×10^{-5}	1.285×10^{-6}
325	1784	0.595	7.432×10^{-5}	2.190×10^{-6}
400	1605	—	—	—

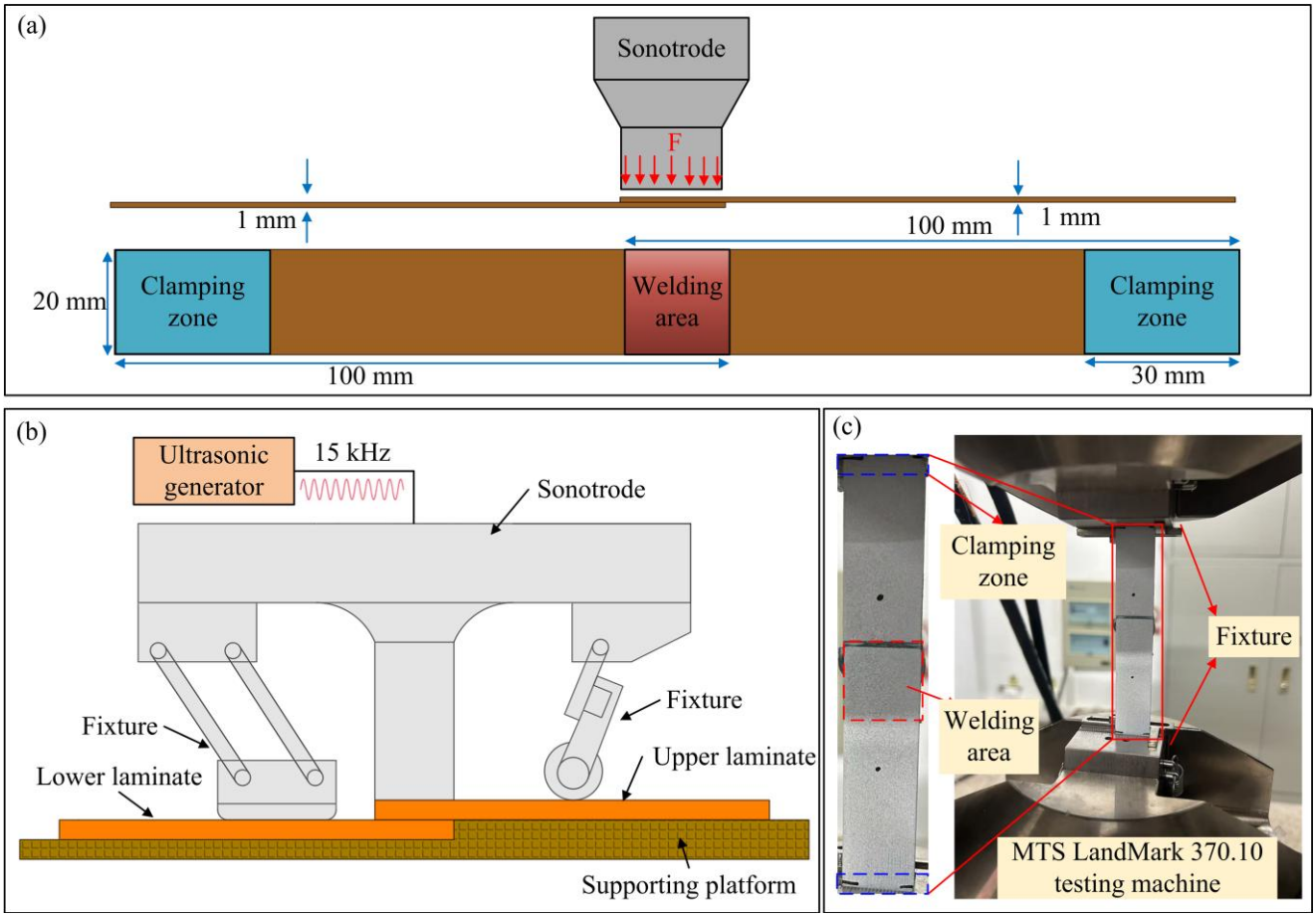

Fig. 2 (a) Specimen dimensions and joint configuration; (b) ultrasonic welding apparatus; (c) single-lap shear testing setup

2.2 Ultrasonic welding equipment and process parameters

Welding was performed using a TK-HJ-CL3 ultrasonic welding system for thermoplastic composite components, supplied by Changzhou Tanke Intelligent Equipment Co., Ltd., China. The system comprised an ultrasonic generator, transducer, booster, sonotrode, and support platform. Its operating frequency was 15 kHz, with a maximum welding force of 300 N and a maximum amplitude of 20 μm. The sonotrode had a flat circular end face with a diameter of 30 mm, as shown in Fig. 2(b). All amplitudes reported here are single-sided amplitudes, defined as the displacement from the vibration center to the maximum position. Electrical signals were converted into mechanical vibration by the transducer and transmitted to the laminates through the booster and sonotrode. Vibration was parallel to the overlap interface. The normal welding force and tangential vibration jointly heated the directly contacting surfaces and produced local bonding.

A one-factor-at-a-time design compared joint behavior across welding force, amplitude, and time series. The baseline condition was 150 N, 12 μm, and 500 ms. One parameter was varied while the other two remained at their baseline values, as listed in Table 3. The three series shared the same baseline condition, resulting in 10 distinct parameter combinations. Lap shear testing and fracture-surface examination were performed on the tested joints. Selected representative joints additionally underwent industrial CT scanning before mechanical testing. For these CT-scanned joints, internal interfacial features were related to load-bearing performance and fracture morphology.

Table 3. One-factor-at-a-time experimental parameters

Parameter series	Variable	Levels	Fixed parameters
Welding force	Force / N	100, 150, 200, 250	Amplitude 12 μm; time 500 ms
Amplitude	Amplitude / μm	9, 12, 15, 18	Force 150 N; time 500 ms
Welding time	Time / ms	500, 650, 800, 1000	Force 150 N; amplitude 12 μm

2.3 Mechanical testing and interfacial characterization

Single-lap shear tests evaluated the load-bearing performance of CF/PEEK joints produced under different welding conditions. Testing was conducted at room temperature using an MTS LandMark 370.10 universal testing machine with a maximum load capacity of 100 kN. Wedge grips held specimens over a gripping length of 30 mm. Single-lap joints are geometrically eccentric, which can introduce bending and specimen misalignment during loading [28]. CF/PEEK tabs matching the laminate thickness were therefore placed at both specimen ends to align the specimen axis with the loading direction. Displacement-controlled loading was applied with one grip fixed and the other moving at 1 mm/min until complete failure of the welded region.

The maximum load recorded during testing was used to calculate the apparent lap shear strength (LSS):

$$\mathrm{LSS} = \frac{F_{\max}}{A_f} = \frac{F_{\max}}{bl} \qquad (1)$$

Here, $F_{\max}$ is the maximum load before joint failure, in N, and A_f is the nominal overlap area, in mm^2. The overlap width b and length l were both 20 mm; thus, A_f was 400 mm^2. LSS is calculated from the nominal overlap area and represents overall joint load-bearing performance rather than local shear strength within the effective bonded region. One independent joint was tested for each welding condition (n = 1). LSS values were used to compare the tested joints, without assessing process repeatability or statistical significance.

Before lap shear testing, selected representative intact joints were scanned nondestructively using a METROTOM 1500 industrial CT system (ZEISS, Germany). The focal spot size and reconstructed voxel size were both 7 μm; the detector pixel size was 139 μm. Reconstructed sections revealed unbonded gaps, local pores, and resin extrusion within the overlap region. Interfacial continuity was compared at the observed section locations.

After lap shear testing, fracture surfaces were examined using an RH-2000 three-dimensional digital microscope (HIROX, Japan). Observations identified unbonded regions, resin residue, matrix fracture, and exposed fibers. For the CT-scanned joints, fracture-surface features were related to CT sections and LSS measurements from the same joint to examine local bonding conditions and load-bearing performance.

Areas were estimated from macroscopic fracture-surface images to compare representative joints produced under different conditions. The red outlines in Fig. 8 identify effective fracture-surface regions based on resin residue, material tearing, and visible bonding traces. The effective fracture-surface area fraction was calculated as the effective-region pixel area divided by the total pixel area of the selected reference region: $R_e = N_e/N_{\mathrm{ref}} \times 100\%$. Here, N_e is the effective-region pixel area within the reference region, and N_{ref} is the total reference-region pixel area. This metric describes the coverage of bonding and failure traces on the fractured surfaces. It was used to compare fracture-surface features, while LSS based on the nominal overlap area represented overall load-bearing performance.

3 Finite element methods

3.1 Theoretical model

In tangential ultrasonic welding, the normal force maintains interfacial contact, while tangential vibration produces relative sliding between the contacting surfaces. A coupled thermomechanical model used interfacial frictional dissipation as the heat input to calculate temperature histories and spatial distributions under different loading conditions. The model included interfacial frictional heating without separately introducing bulk viscoelastic heating or molten resin flow. The calculations characterized thermal responses under this assumption; bonding and load-bearing performance were evaluated using CT, fracture-surface observations, and mechanical testing.

In Fig. 3, F_n denotes the normal welding force, and v_{slip} denotes the actual relative sliding velocity between the contacting surfaces. The magnitude of the interfacial frictional shear stress is denoted by τ_f. Frictional heat flux is expressed using the shear stress, relative sliding velocity, and fraction of dissipated energy converted into heat [15]:

$$q_f(x,y,t) = \eta\tau_f(x,y,t)|v_{\text{slip}}(x,y,t)| \qquad (2)$$

Here, q_f is the local frictional heat flux, in W·m^{-2}, and η is the fraction of frictional dissipation converted into heat. The units of τ_f and v_{slip} are Pa and m·s^{-1}, respectively. The coordinates x and y locate positions within the interface, and t denotes time.

A Coulomb friction model described tangential interfacial behavior. Under sliding contact, the frictional shear stress satisfies τ_f = μp, where μ is the friction coefficient and p is the local contact pressure. Values of μ = 0.3 and η = 1.0 were used, converting all frictional dissipation into heat. Local contact pressure and actual sliding velocity were obtained from the contact solution. Their variation with position and time determined the spatial distribution of frictional heating.

A heat partition coefficient of 0.5 distributed frictional heat equally between the upper and lower laminates [15]:

$$q_f^{\text{upper}} = 0.5q_f, q_f^{\text{lower}} = 0.5q_f \qquad (3)$$

Here, q_f^{upper} and q_f^{lower} are the frictional heat fluxes entering the upper and lower laminates, respectively. Heat generated at the interface diffuses into the laminates by conduction. With no other internal heat sources, transient heat conduction within the laminates is described by:

$$\rho C_p(T)\frac{\partial T}{\partial t} = \nabla\cdot[k(T)\nabla T] \qquad (4)$$

Here, ρ is the material density, in kg·m^{-3}, and C_p(T) is the temperature-dependent specific heat capacity, in J·kg^{-1}·K^{-1}. T denotes temperature, and k(T) is the temperature-dependent thermal conductivity, in W·m^{-1}·K^{-1}. The symbols ∇ and ∇· denote the gradient and divergence operators, respectively. A scalar thermal conductivity was used to describe heat conduction.

The finite element analysis used an explicit coupled temperature–displacement formulation in Abaqus. The contact algorithm calculated frictional dissipation from local frictional interactions and actual sliding. Contact heat generation converted this dissipation into heat inputs for the upper and lower laminates. No additional uniform heat flux boundary condition was applied, avoiding duplicate frictional heat input.

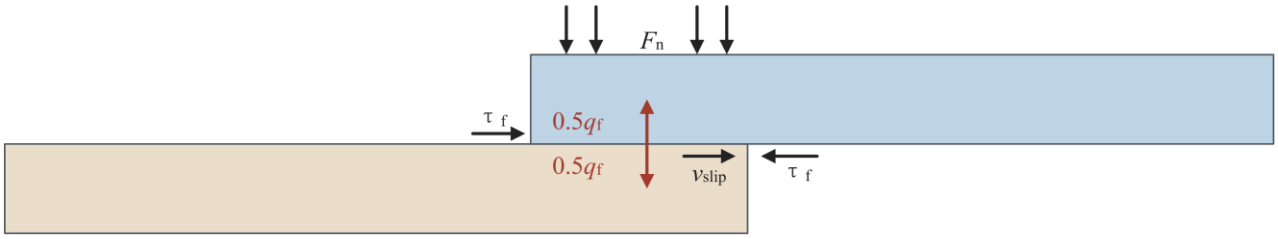

Fig. 3 Schematic of interfacial frictional heating during ultrasonic welding

3.2 Finite element model and boundary conditions

A three-dimensional coupled thermomechanical model of tangential ultrasonic welding without energy directors was developed in Abaqus 2023, as shown in Fig. 4. The upper and lower laminates each measured 100 mm × 20 mm × 1 mm, with a 20 mm × 20 mm overlap matching the experiments. Each laminate comprised eight 0.125 mm prepreg plies in a $[0/90]_{2s}$ lay-up. No energy directors or additional resin layers were placed at the interface. The model retained both laminates and represented loading and vibration through normal pressure and periodic tangential displacement. The sonotrode and support platform were not modeled separately.

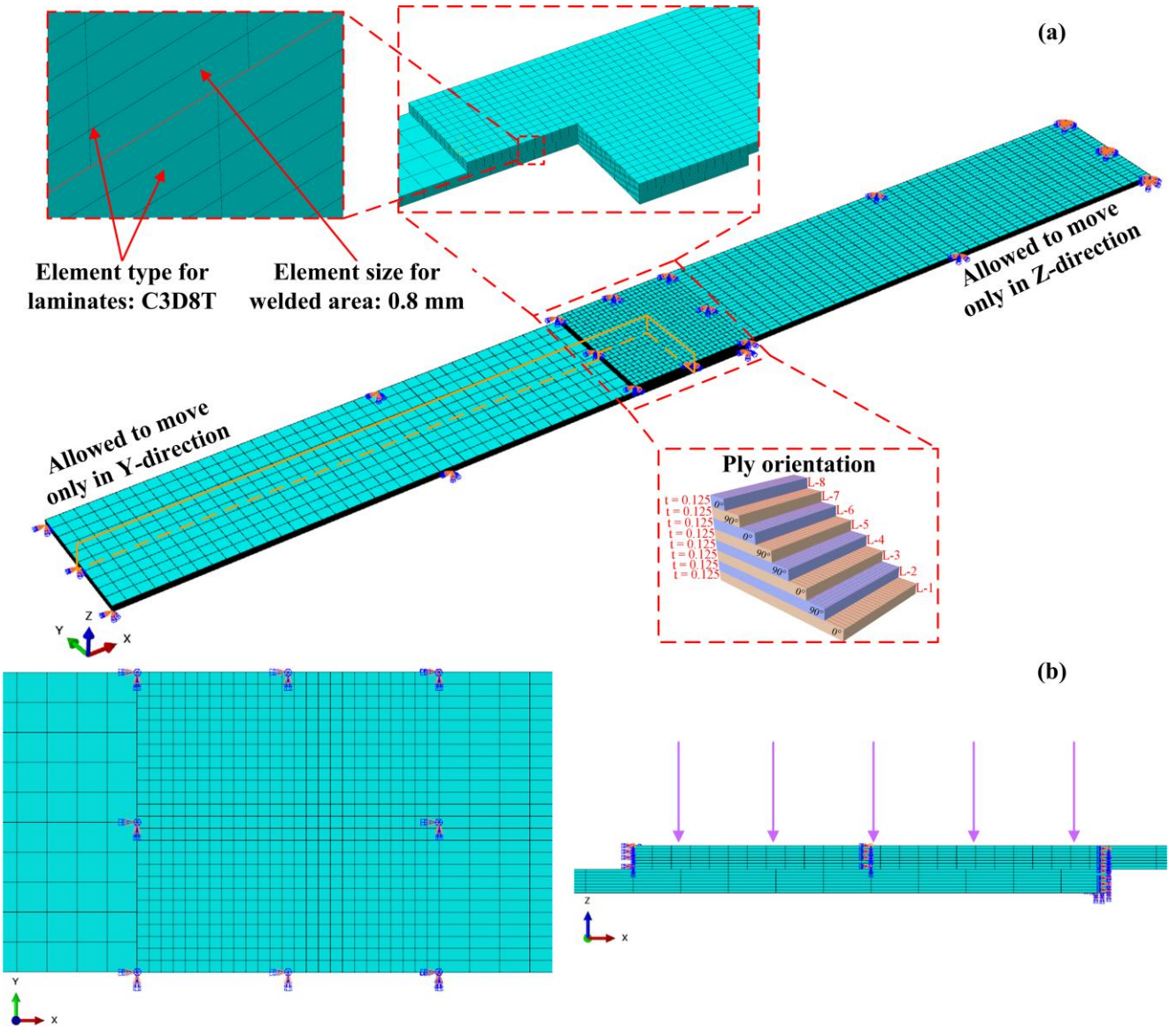

Fig. 4 CF/PEEK ultrasonic welding model: (a) 3D model and local mesh refinement; (b) boundary conditions

Temperature-dependent anisotropic elasticity was used, with local material coordinate systems assigned according to the fiber direction in each ply. Elastic constants and thermophysical properties were taken from Tables 1 and 2, respectively. An explicit coupled temperature–displacement analysis was performed with an initial temperature of 20 °C. Hard contact and a friction coefficient of 0.3 were assigned to the overlap interface. All frictional dissipation was converted into heat and partitioned equally between the contacting surfaces.

During welding, normal pressure was applied to the upper laminate, while periodic tangential displacement was applied to the lower laminate parallel to the overlap interface. The applied pressure was calculated from the welding force and nominal overlap area: $p = Fn / Aw$, with $Aw = 20\ mm \times 20\ mm = 400\ mm^2$. At the baseline condition, a force of 150 N corresponded to 0.375 MPa, and an amplitude of 12 μm corresponded to a displacement amplitude of 0.012 mm. The vibration frequency of 15 kHz corresponded to an angular frequency of 9.4248×10^4 rad/s. Welding force, amplitude, and time for each modeled condition matched Table 3.

The laminates were discretized using C3D8T eight-node three-dimensional coupled temperature–displacement solid elements. A global mesh with local refinement in the welding region was used. The local element size was 0.8 mm to describe the interfacial temperature distribution. All conditions used the same meshing scheme.

3.3 Temperature evolution under a literature reference condition

A reference case was established using the experimental conditions reported by Bonmatin et al. [12]. The calculated temperature history was compared with their measured results. Their joints contained PEI interfacial layers, whereas the present welding experiments used CF/PEEK laminates in direct contact. The comparison addressed heating, peak temperature, and cooling under the literature reference condition. Temperatures reported for the directly contacting system in this study are model calculations.

The reference specimens measured 100 mm × 25 mm × 2 mm and comprised 16 plies, each 0.125 mm thick, in a $[0/90]_4s$ lay-up [12]. The welding interface contained three PEI films, each 0.25 mm thick. Two films were placed on the mating laminate surfaces, and the third was positioned between the specimens, giving an initial PEI thickness of 0.75 mm. A K-type thermocouple embedded in the PEI layer recorded interfacial temperature during welding.

The reference frequency, welding force, and peak-to-peak amplitude were 20 kHz, 500 N, and 32 μm, respectively. For the sinusoidal displacement loading used here, this peak-to-peak amplitude corresponds to a single-sided amplitude of 16 μm. Temperature histories were referenced to the onset of ultrasonic vibration. The comparison covered heating, the temperature peak, and cooling after vibration stopped.

Figure 5 shows similar rapid heating, temperature peaks, and subsequent cooling in the calculated and literature-measured curves. This reference comparison illustrates the model description of the main temperature-evolution trends. Subsequent calculations examine temperature distributions and parameter responses at directly contacting interfaces.

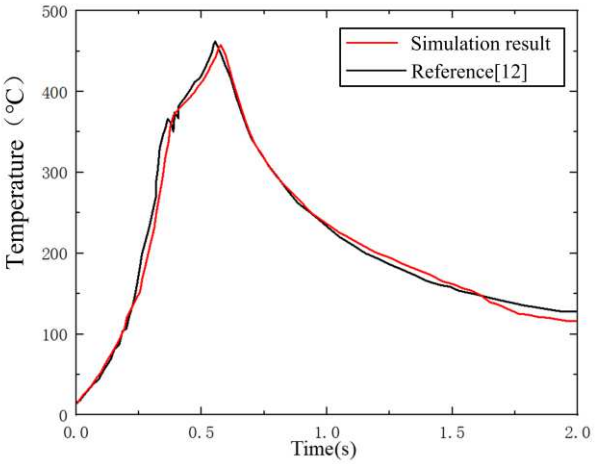

Fig. 5 Calculated and literature-measured temperature histories under the reference conditions reported in [12]

4 Results and discussion

4.1 Interfacial thermal response in the frictional heating model

Figures 6 and 7 show the calculated interfacial temperature fields and temperature histories at an interface edge, respectively. Macroscopic bonding traces are considered alongside these results to examine the spatial characteristics of the thermal response.

At amplitudes of 12 and 15 μm, high-temperature regions were concentrated mainly near the overlap edges and local contact positions, producing nonuniform distributions (Fig. 6). The calculated edge temperature peak was higher at 15 μm than at 12 μm. This trend is consistent with the relationship between relative sliding and heat input in the frictional heating model. The corresponding joints also exhibited different macroscopic bonding traces. These observations highlight local spatial distributions when relating thermal response to bonding conditions.

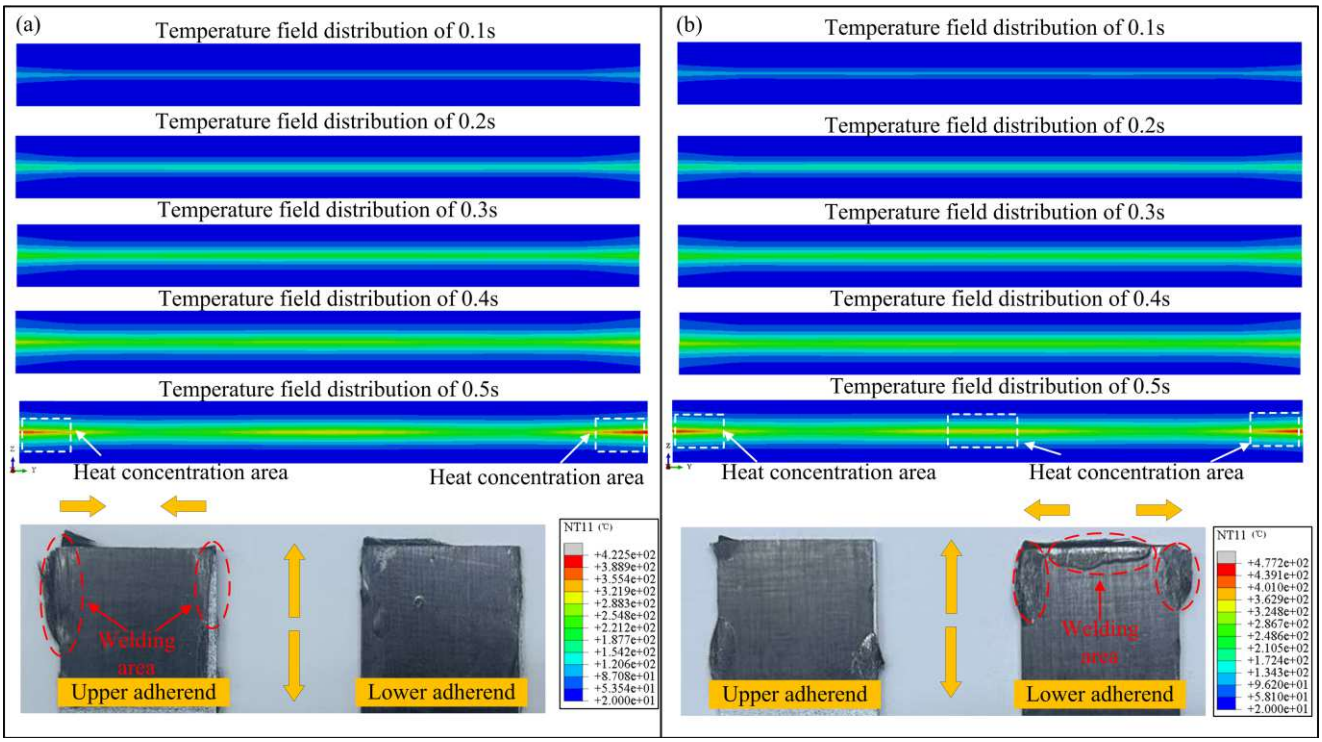

Fig. 6 Calculated interfacial temperature fields and corresponding joint morphologies at (a) 12 μm and (b) 15 μm

The calculated edge temperature histories in Fig. 7 include heating and cooling stages for all conditions. At fixed welding force and time, increasing amplitude corresponded to a higher edge temperature peak. At a fixed

frequency, displacement amplitude affects the relative interfacial motion velocity. Actual sliding and frictional shear stress obtained from the contact solution jointly determine local heat input [9,12].

Welding force contributes to frictional heating through contact pressure and sliding conditions, while welding time determines the duration of vibration loading. The three parameters therefore affect the modeled thermal response through contact conditions, displacement amplitude, and loading duration, respectively.

Figures 6 and 7(b) associate increasing amplitude with a higher edge temperature peak, while high-temperature regions remain locally concentrated. The following analysis combines effective fracture-surface regions, CT sections, and microscopic fracture features to examine bonding and load-bearing performance under different heat-input conditions.

Interface-design studies provide context for this local thermal response. Investigations using embossed and variable-flexibility energy directors relate interfacial temperature distributions to welding quality [21,23]. In the present directly contacting interface, high-temperature regions concentrate near the overlap edges, indicating the relevance of the spatial distribution of heat input when interpreting parameter effects. Fracture surfaces and CT sections are subsequently used to examine the bonding features associated with these local thermal responses.

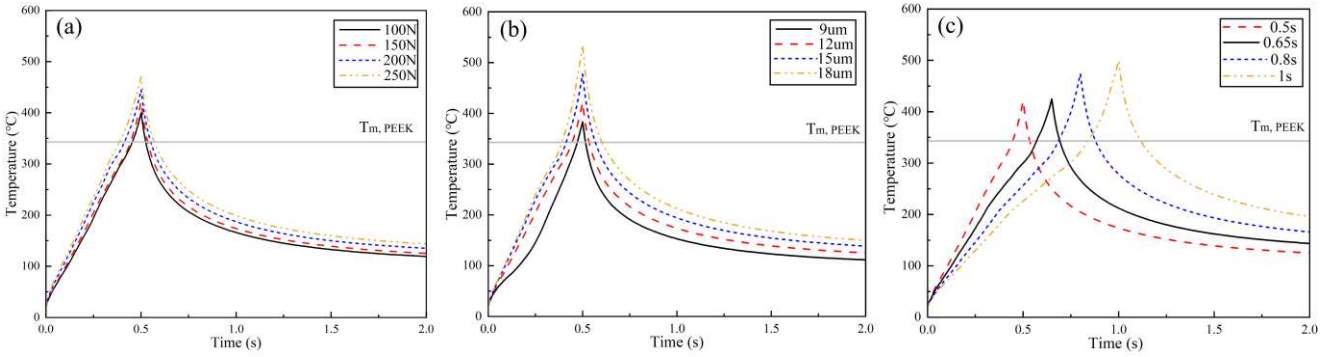

Fig. 7 Calculated interface-edge temperature histories for the (a) welding force, (b) amplitude, and (c) time series

4.2 Load-bearing performance and effective fracture-surface coverage

Figures 8 and 9 relate macroscopic fracture surfaces to apparent lap shear strength. Resin residue, material tearing, and bonding traces indicate failure characteristics across different regions after loading. The effective fracture-surface area fraction, estimated as defined in Section 2.3, compares the coverage of these features.

The baseline condition (150 N, 12 μm, 500 ms) had an effective fracture-surface area fraction of approximately 16.0%. In the force series, the values at 100, 200, and 250 N were 9.6%, 10.1%, and 10.9%, respectively. In the amplitude series, the values at 9, 15, and 18 μm were 9.4%, 19.1%, and 13.2%, respectively. In the time series, the values at 650, 800, and 1000 ms were 20.3%, 46.0%, and 32.9%, respectively. The 800 ms joint had the largest effective fracture-surface area fraction among the examined joints. All fractions used the selected image reference region as the denominator.

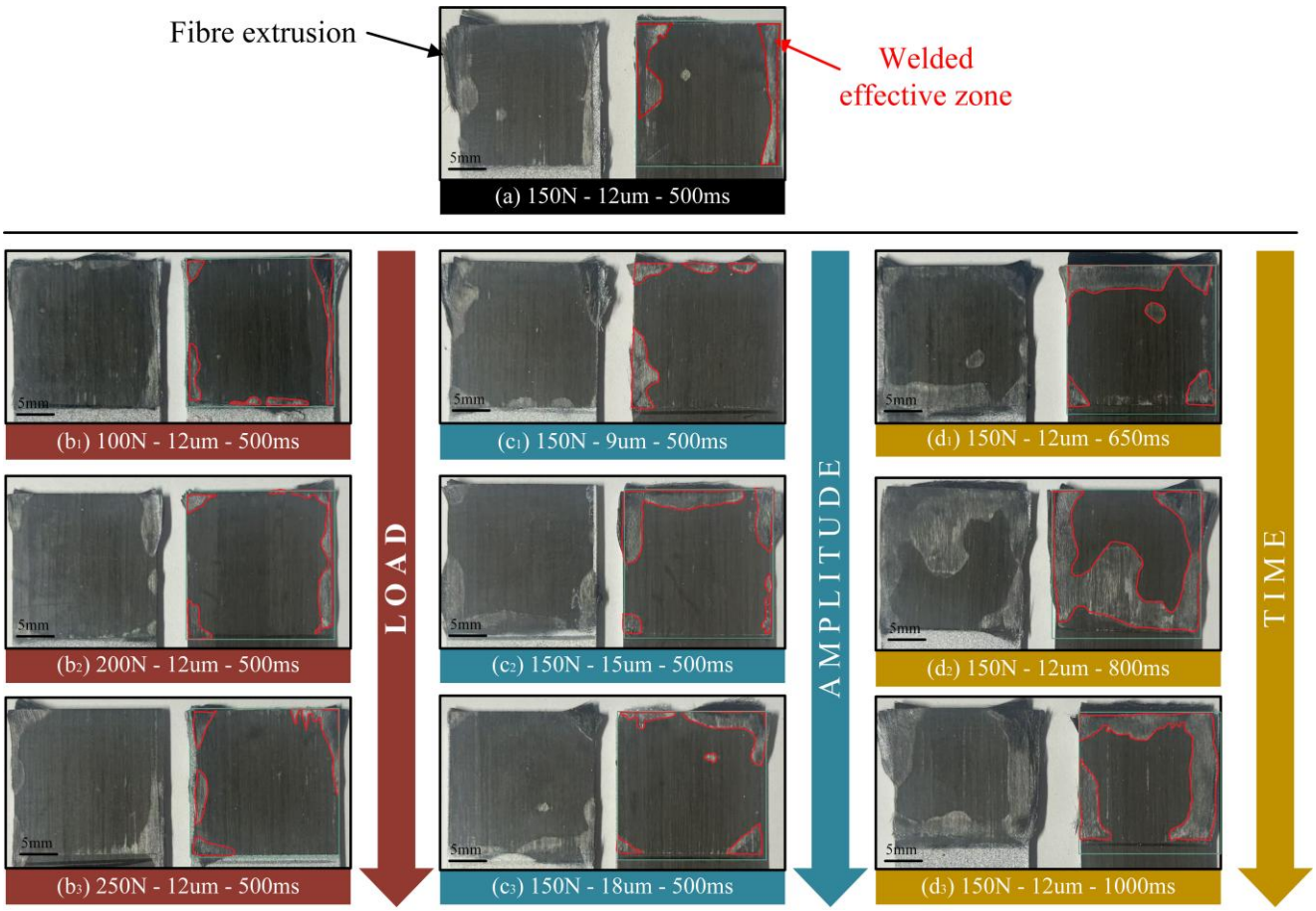

Fig. 8 Macroscopic fracture surfaces and effective regions (outlined regions) under different welding conditions

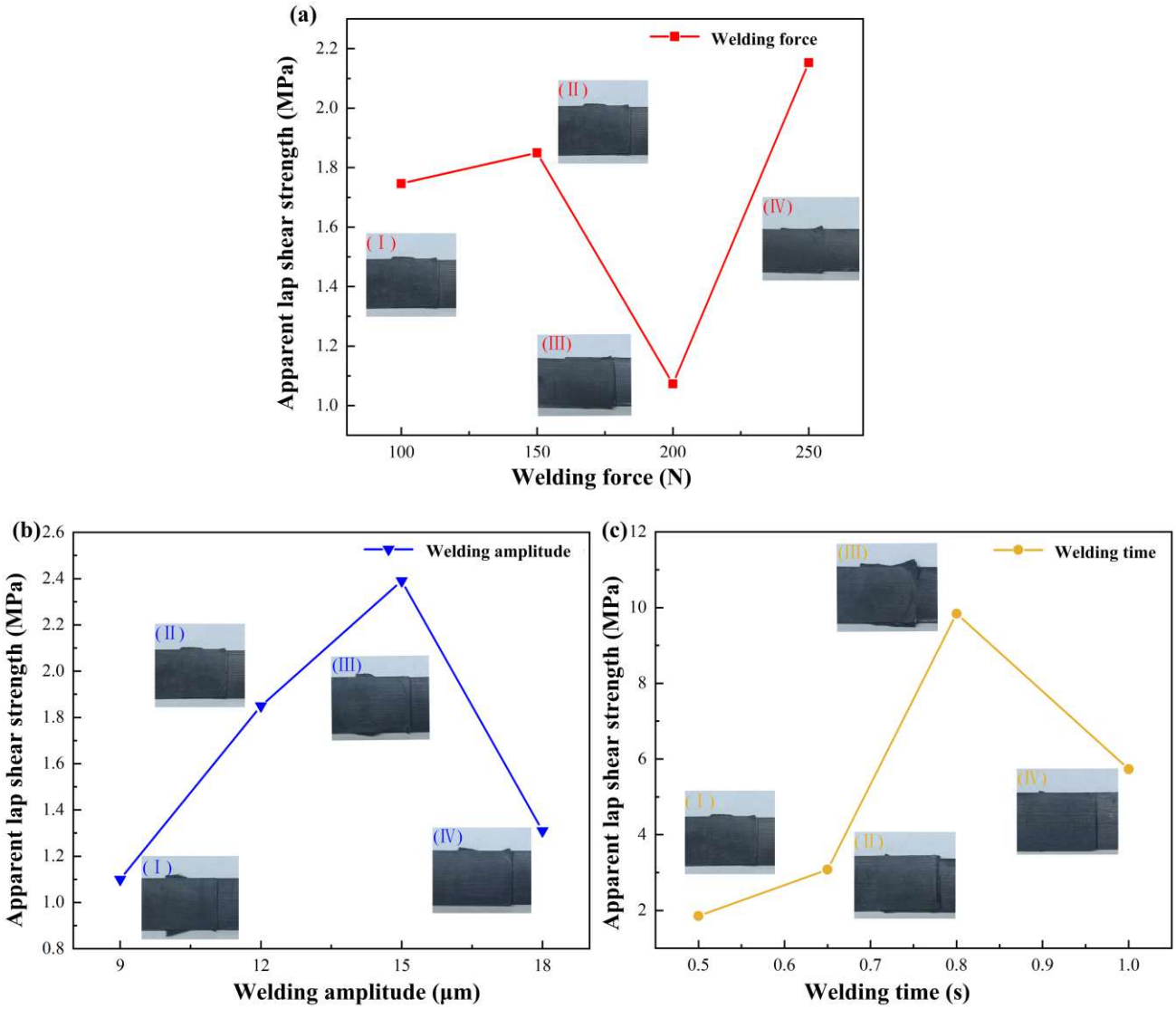

Fig. 9 Apparent lap shear strengths of CF/PEEK joints for the (a) force, (b) amplitude, and (c) time series; each point represents one independent joint

Strength varied nonmonotonically in the force series. The 250 N joint reached the highest measured strength in this series, 2.15 MPa (Fig. 9(a)). Its effective fracture-surface area fraction was 10.9%, compared with 16.0% for the 150 N joint. This comparison shows different changes in effective fracture-surface coverage and overall load-bearing performance. Local bonding conditions and their spatial distribution therefore provide additional information for interpreting differences between these joints. CT and microscopic fracture-surface observations supply the corresponding structural features.

At 150 N and 500 ms, strength increased as amplitude rose from 9 to 15 μm, reaching the series maximum of 2.39 MPa at 15 μm. The 18 μm joint had a strength of 1.31 MPa (Fig. 9(b)). Effective fracture-surface area fractions at 9, 15, and 18 μm were 9.4%, 19.1%, and 13.2%, respectively, matching the direction of strength changes. The 15 μm joint combined greater effective fracture-surface coverage with higher load-bearing performance. The amplitude series thus exhibited corresponding changes in fracture-surface coverage and strength.

At 150 N and 12 μm, extending welding time from 500 to 800 ms increased the effective fracture-surface area fraction from 16.0% to 46.0%. The 800 ms joint reached an apparent lap shear strength of 9.84 MPa (Fig. 9(c)). The 1000 ms joint had an area fraction of 32.9% and a strength of 5.73 MPa. Effective fracture-surface coverage and load-bearing performance changed in the same direction across the time series. The 800 ms condition combined greater coverage with the highest measured strength among the tested conditions.

The ring-focused CF/PEEK welding study related an enlarged weld area to increased joint strength by modifying local support conditions [25]. The present effective fracture-surface area fraction describes the coverage of bonding and failure traces after loading and differs in definition from weld area. The corresponding changes in the amplitude and time series, together with the different area–strength relationship in the force series, indicate that this coverage metric should be interpreted alongside CT interfacial continuity and local failure features when assessing load-bearing differences.

4.3 Interfacial continuity and local defects in CT sections

Figure 10(a1–a3) shows internal interfacial features in the force series. The 100 N joint exhibited pronounced unbonded gaps. Gaps were reduced in the observed section of the 150 N joint, with improved interfacial continuity. Local pores and resin extrusion were visible in the 250 N joint. Its higher measured strength coexisted with local defects. These observations supplement the internal structural evidence for interpreting the area–strength relationship in the force series.

In the amplitude series, the observed section of the 9 μm joint contained unbonded gaps. The 15 μm joint showed fewer gaps and a more continuous interface. Local defects and resin extrusion were visible at 18 μm (Fig. 10(b1–b3)). Greater effective fracture-surface coverage, a more continuous observed interface, and higher strength occurred together in the 15 μm joint.

In the time series, the 500 ms joint contained local gaps, whereas fewer unbonded gaps were visible in the observed section at 800 ms. Local gaps and resin extrusion appeared again at 1000 ms (Fig. 10(c1–c3)). The 800 ms joint combined greater effective fracture-surface coverage with higher strength. This correspondence connects fracture-surface traces to internal interfacial continuity within that joint.

Macroscopic fracture-surface areas characterize effective-region coverage, whereas CT sections characterize internal interfacial conditions. In the amplitude and time series, greater coverage and more continuous observed interfaces corresponded to higher load-bearing performance. The different relationship in the force series emphasizes the role of local bonding conditions in joint analysis.

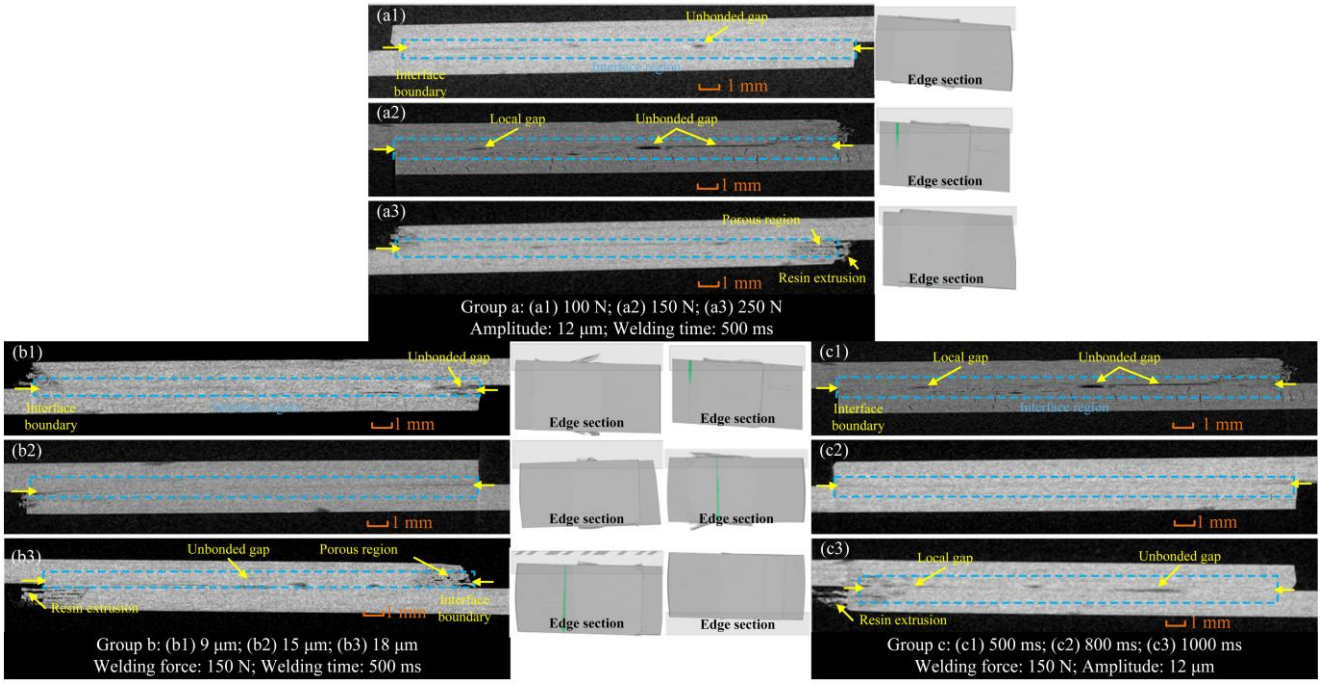

Fig. 10 Industrial CT sections near the overlap edges of representative CF/PEEK joints under different welding conditions and the corresponding section locations

4.4 Fracture morphology and local load-transfer features

Microscopic fracture observations distinguished unbonded regions from failure features in regions involved in load transfer (Fig. 11). Panels (a1–a4), (b1–b4), and (c1–c4) represent the force, amplitude, and time series, respectively. Resin residue, matrix fracture, and fiber damage indicate material failure within locally bonded regions during loading. Unbonded regions lacked continuous bonding traces on the fracture surfaces.

In the force series, the 100 N joint contained pronounced unbonded regions (Fig. 11(a1)). Exposed fibers and local fiber fracture were observed under the other conditions, indicating contributions from interfacial separation and local material failure. The porous fracture-surface region of the 250 N joint corresponded to local pores in its CT section (Fig. 11(a4)). These observations provide complementary information on local bonding under this condition.

In the amplitude series, the 9 μm joint showed unbonded regions, resin residue, and exposed fibers (Fig. 11(b1)). Resin residue and local fiber fracture at 15 μm indicated matrix and fiber damage within some bonded regions (Fig. 11(b3)). The 18 μm joint retained unbonded regions and exposed fibers (Fig. 11(b4)). Together with macroscopic area estimates and CT sections, these features associate the higher strength at 15 μm with greater coverage and interfacial continuity.

In the time series, locally bonded regions in the 500 ms joint exhibited matrix fracture and fiber damage, alongside retained unbonded regions (Fig. 11(c1)). At 800 ms, effective fracture-surface coverage expanded and the observed CT interface became more continuous. Microscopic fracture observations also revealed local pores (Fig. 11(c3)). Porous regions in the 1000 ms fracture surface corresponded to resin extrusion and local gaps in CT sections (Fig. 11(c4)). Macroscopic coverage and local interfacial features together describe the different bonding conditions of the 800 and 1000 ms joints.

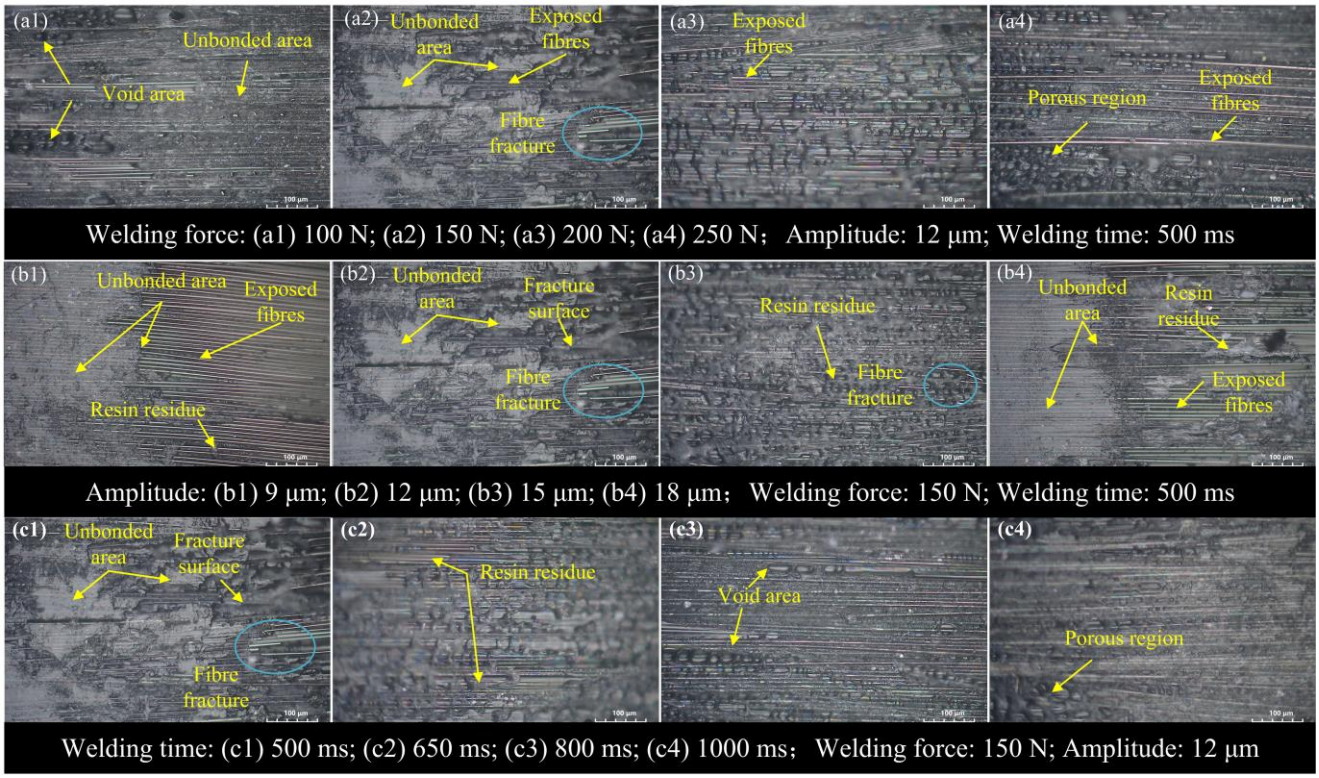

Fig. 11 Fracture morphologies of CF/PEEK ultrasonic welded joints produced under different welding conditions

Macroscopic fracture surfaces, CT sections, and microscopic fracture observations describe joint conditions through coverage, internal continuity, and local failure features, respectively. Fracture of the tested joints involved interfacial separation, matrix failure, and fiber damage. These features provide structural context for load-bearing differences within the parameter series.

4.5 Bonding assessment and process analysis

The three parameter series support considering effective fracture-surface coverage together with internal interfacial conditions in process analysis. In the amplitude and time series, greater coverage and improved continuity in the observed sections corresponded to higher strength. The force series exhibited a different area–strength relationship. Combining macroscopic area estimates, CT sections, and microscopic fracture observations connects differences between welding conditions to specific bonding and defect features.

Studies using PEI energy directors regulate bond formation through interfacial configuration and process control [12,13]. Wang et al. subsequently achieved CF/PEI welding without additional energy directors by co-consolidating an extra resin layer [26]. Their approach modified interfacial resin supply. The present work uses directly contacting CF/PEEK interfaces without additional resin layers and relates effective fracture-surface coverage, interfacial continuity, and local defects to load-bearing performance under tangential vibration. Parameter comparisons refer to the one-factor-at-a-time conditions in Table 3, and thermal response analysis uses the frictional heating model described in Section 3.

5 Conclusions

This study combined frictional heating calculations, lap shear testing, industrial CT, and fracture-surface observations for tangential ultrasonic welding of CF/PEEK without separate energy directors. Joint load-bearing performance was related to effective fracture-surface coverage and local bonding conditions. The main conclusions are as follows:

(1) Frictional heating calculations showed spatially nonuniform interfacial temperatures, with high-temperature regions concentrated mainly near the overlap edges. Increasing amplitude raised the edge temperature peak, characterizing the local thermal response under the modeled loading conditions.

(2) Among the tested joints, strength first increased and then decreased in the amplitude and time series, whereas the force series varied nonmonotonically. At 150 N, 12 μm, and 800 ms, the apparent lap shear strength was 9.84 MPa, the highest measured value among the tested conditions. Extending welding time to 1000 ms gave 5.73 MPa. The highest measured strengths in the force and amplitude series were 2.15 MPa at 250 N and 2.39 MPa at 15 μm, respectively.

(3) Effective fracture-surface area fraction and strength changed in the same direction in the amplitude and time series. The area fractions at 800 and 1000 ms were 46.0% and 32.9%, respectively; the force series exhibited a different area–strength relationship. CT and microscopic fracture observations identified unbonded gaps, local pores, and matrix and fiber damage. Effective fracture-surface coverage, interfacial continuity, and local defects together provide structural evidence for assessing joint quality in welding without energy directors.

Author contributions

Zhongliang Cao: Conceptualization, research design, methodology, and critical manuscript review. Fanyang Liu: Experimental investigation, simulation analysis, and writing the original draft. Leiming Chen: Data curation, analysis, and manuscript revision. Jiazeng Pan: Data analysis, interpretation of results, and manuscript revision. Zhichuan Lin: Validation and analysis of interfacial bonding and failure behavior. Jintao Gu: Research discussion, manuscript review, and language editing.

Statements and Declarations

Ethical considerations

Not applicable. This study did not involve human participants or animals.

Consent to participate

Not applicable.

Consent for publication

Not applicable.

Declaration of conflicting interest

The authors declared no potential conflicts of interest with respect to the research, authorship, and/or publication of this article.

Data availability

The data supporting the findings of this study are available from the corresponding author on reasonable request.

References

1. Liu JM, Quan D, Scarselli G, et al (2025) Developments and future prospects of welding technology for carbon fiber thermoplastic composites. Compos Part B Eng 297:112314. https://doi.org/10.1016/j.compositesb.2025.112314
2. Takeda SI, Kugi D, Hoshi H, et al (2025) Influence of preheating on ultrasonic welding of CF/PEEK composite laminates. Compos Struct 373:119668. https://doi.org/10.1016/j.compstruct.2025.119668
3. Tilahun S, Vijayakumar MD, Ramesh Kannan C, et al (2020) A review on ultrasonic welding of various materials and their mechanical properties. IOP Conf Ser Mater Sci Eng 988(1):012113. https://doi.org/10.1088/1757-899X/988/1/012113
4. Bhudolia SK, Gohel G, Leong KF, et al (2020) Advances in ultrasonic welding of thermoplastic composites: A review. Materials 13(6):1284. https://doi.org/10.3390/ma13061284
5. Liu Z, Li Y, Liu Z, et al (2023) Ultrasonic welding of metal to fiber-reinforced thermoplastic composites: A review. J Manuf Process 85:702-712. https://doi.org/10.1016/j.jmapro.2022.12.001
6. Arumugam A, Pramanik A (2024) A review on the recent trends in forming composite joints using spot welding variants. J Compos Sci 8(4):155. https://doi.org/10.3390/jcs8040155
7. Tsiangou E, Teixeira de Freitas S, Fernandez Villegas I, et al (2019) Investigation on energy director-less ultrasonic welding of polyetherimide (PEI)-to-epoxy-based composites. Compos Part B Eng 173:107014. https://doi.org/10.1016/j.compositesb.2019.107014
8. Tolunay MN, Dawson PR, Wang KK (1983) Heating and bonding mechanisms in ultrasonic welding of thermoplastics. Polym Eng Sci 23(13):726-733. https://doi.org/10.1002/pen.760231307
9. Levy A, Le Corre S, Fernandez Villegas I (2014) Modeling of the heating phenomena in ultrasonic welding of thermoplastic composites with flat energy directors. J Mater Process Technol 214(7):1361-1371. https://doi.org/10.1016/j.jmatprotec.2014.02.009
10. Tao W, Su X, Wang H, et al (2019) Influence mechanism of welding time and energy director to the thermoplastic composite joints by ultrasonic welding. J Manuf Process 37:196-202. https://doi.org/10.1016/j.jmapro.2018.11.002
11. Liu J, Yue D, Wang X, et al (2024) Effects of welding displacement and energy director thickness on the ultrasonic welding of epoxy-to-polyetherimide based hybrid composite joints. Compos Sci Technol 257:110810. https://doi.org/10.1016/j.compscitech.2024.110810
12. Bonmatin M, Chabert F, Bernhart G, et al (2022) Ultrasonic welding of CF/PEEK composites: Influence of welding parameters on interfacial temperature profiles and mechanical properties. Compos Part A Appl Sci Manuf 162:107074. https://doi.org/10.1016/j.compositesa.2022.107074
13. Korycki A, Carassus F, Garnier C, et al (2026) Comparison and optimization of ultrasonic welding parameters in time and displacement mode for CF/PEEK composite with integrated energy director. Int J Adv Manuf Technol 144:2987-3000. https://doi.org/10.1007/s00170-026-18110-9

14. Tsiangou E, De Freitas ST, Benedictus R, et al (2021) On the sensitivity of the ultrasonic welding process of epoxy- to polyetheretherketone (PEEK)-based composites to the welding force and amplitude of vibrations. Compos Part C Open Access 5:100141. https://doi.org/10.1016/j.jcomc.2021.100141

15. Koyanagi J, Takamura M, Wakayama K, et al (2022) Numerical simulation of ultrasonic welding for CFRP using energy director. Adv Compos Mater 31(4):428-441. https://doi.org/10.1080/09243046.2022.2031376

16. Hua Z, Ren H, Zhang R, et al (2025) Numerical simulation and experimental study of ultrasonic welding of CF/PEEK composites. J Appl Polym Sci 142(30):e57207. https://doi.org/10.1002/app.57207

17. Zhao T, Zhao Q, Wu W, et al (2021) Enhancing weld attributes in ultrasonic spot welding of carbon fibre-reinforced thermoplastic composites: Effect of sonotrode configurations and process control. Compos Part B Eng 211:108648. https://doi.org/10.1016/j.compositesb.2021.108648

18. Ren YY, Han B, Yan QY, et al (2025) High-performance ultrasonic welding of continuous carbon fiber reinforced polycarbonate composites: Synergizing simulation and experimentation. Compos Struct 372:119555. https://doi.org/10.1016/j.compstruct.2025.119555

19. Wang X, Quan D, Yue D, et al (2024) Realizing ultrahigh strength and excellent stability of ultrasonically welded joints upon co-consolidating an extra resin layer (eRL) on the thermoplastic composites. Compos Part A Appl Sci Manuf 187:108475. https://doi.org/10.1016/j.compositesa.2024.108475

20. Wang J, Zhang J, Cheng J, et al (2026) The analysis of joint failure mode and effects of ultrasonic welding parameters on the mechanical properties of CF/PEEK composite joints. Polym Compos 47(12):11429-11443. https://doi.org/10.1002/pc.71032

21. Wang T, Zhang Z, Ao S, et al (2024) Ultrasonic welding of continuous carbon fiber reinforced PEEK with embossed energy directors. J Manuf Process 131:256-269. https://doi.org/10.1016/j.jmapro.2024.09.004

22. Li Y, Liu Z, Liao W, et al (2026) High-Quality Spot and Continuous Ultrasonic Welding of Carbon Fiber Reinforced Polyetheretherketone (CF/PEEK) Composites Using PEEK Mesh Energy Directors. Appl Compos Mater 33:46. https://doi.org/10.1007/s10443-025-10419-0

23. Liu J, Quan D, Pan J, et al (2025) Enhancing welding-line uniformity and joint strength of ultrasonically welded CF/epoxy-CF/PEI hybrid joints using variable-flexibility energy directors. J Manuf Process 135:69-81. https://doi.org/10.1016/j.jmapro.2025.01.032

24. Yang Y, Ma Z, Zhu Y, et al (2026) Toward high-quality ultrasonic welding of CF/PEEK by tailoring the crystallinity of the energy director. J Manuf Process 171:299-317. https://doi.org/10.1016/j.jmapro.2026.05.042

25. Liu Y, Li J, Wu Z (2026) Ring-Focused Ultrasonic Welding of CF/PEEK Composites Without Energy Director. J Mater Eng Perform 35:3850-3862. https://doi.org/10.1007/s11665-025-11865-4

26. Wang X, Quan D, Liu J, et al (2025) Towards ultrasonic welding of robust thermoplastic composite joints without the use of energy directors. Compos Part B Eng 302:112561. https://doi.org/10.1016/j.compositesb.2025.112561

27. Victrex plc (2018) VICTREX PEEK polymer properties guide. Victrex plc, Thornton Cleveleys. https://www.victrex.com/-/media/downloads/technical-guides/victrex-product-guide-victrex-peek-properties-en-09-2018.pdf. Accessed 21 Sep 2026

28. Brito CBG, Teuwen J, Dransfeld CA, et al (2022) The effects of misaligned adherends on static ultrasonic welding of thermoplastic composites. Compos Part A Appl Sci Manuf 155:106810. https://doi.org/10.1016/j.compositesa.2022.106810